

Article

Micro Photosynthetic Power Cell Array for Energy Harvesting: Bio-Inspired Modeling, Testing and Verification

Kirankumar Kuruvinashetti ¹, Shanmuga Sundaram Pakkiriswami ², Dhilippan M. Panneerselvam ¹ and Muthukumaran Packirisamy ^{1,*} 

¹ Optical Bio Microsystems Laboratory, Department of Mechanical, Industrial and Aerospace Engineering, Concordia University, Montreal, QC H3G 1M8, Canada; k_kuruvi@encs.concordia.ca (K.K.); dhilippan.mamsapurampanneerselvam@concordia.ca (D.M.P.)

² Department of Biochemistry and Molecular Biology, Dalhousie Medicine New Brunswick (DMNB), Dalhousie University, Saint John, NB E2L 4L5, Canada; sn374151@dal.ca

* Correspondence: pmuthu@alcor.concordia.ca

Abstract: A micro-photosynthetic power cell (μ PSC) generates electricity through the exploitation of living photosynthetic organisms through the principles of photosynthesis and respiration. Modeling such systems will enhance insights into the μ PSC that can be employed to design real-time applications from μ PSC. In this study, the bio-inspired electrical equivalent modeling of the array of μ PSC is elucidated. The model is validated for array configurations of the micro-photosynthetic power cells. The developed arrayed model foresees the steady-state response at various electrical loadings. The polarization characteristics of the current-voltage (I-V) and current-power (I-P) characteristics of the array of μ PSC in series and parallel, and their combinations in series and parallel connected μ PSCs were validated with the experimental results. From this analysis, it is predicted that the arraying of the μ PSC in the combination of series and parallel is the optimal array strategy to obtain the desired voltage and current from the μ PSC such that it can be used to power real-time low and ultra-low power devices.

Keywords: modeling bio-photoelectrochemical cells; bio-photovoltaics; photosynthesis; energy harvesting; sustainable energy



Citation: Kuruvinashetti, K.; Pakkiriswami, S.S.; M. Panneerselvam, D.; Packirisamy, M. Micro Photosynthetic Power Cell Array for Energy Harvesting: Bio-Inspired Modeling, Testing and Verification. *Energies* **2024**, *17*, 1749. <https://doi.org/10.3390/en17071749>

Academic Editor: Bartłomiej Iglński

Received: 30 October 2023

Revised: 15 December 2023

Accepted: 17 December 2023

Published: 5 April 2024



Copyright: © 2024 by the authors. Licensee MDPI, Basel, Switzerland. This article is an open access article distributed under the terms and conditions of the Creative Commons Attribution (CC BY) license (<https://creativecommons.org/licenses/by/4.0/>).

1. Introduction

Powering the rising necessity of energy from fossil fuels leads to catastrophic consequences, such as global warming and climate change [1]. In addition to these environmental consequences, the depletion of fossil fuels demands the need to find alternative power sources. To this effect, the various renewable energy sources that can produce power in different ranges are in demand [1]. Scaling down high power sources to low power applications leads to an increase in the size of the devices due to the add-on of power converters [2]. Moreover, tremendous growth in miniaturized recent technologies such as IoT sensors, and low-power devices has increased the necessity for low-power sustainable power sources demand [3].

In this context, micro-photosynthetic power cells (μ PSC) are a sustainable option for low- and ultra-low power applications. The μ PSC is a microbial fuel cell that generates electricity through the exploitation of living photosynthetic microorganisms or cells. In the presence of light through photosynthesis, photosynthetic microorganisms release electrons through water-splitting reactions. In dark conditions, by the respiration principle, through catabolic activity, electrons are released. These released electrons are harvested through efficiently designed electrochemical cells [4–8]. The significant benefit of the μ PSC is that they consist of living photosynthetic microorganisms; these microorganisms have self-repair ability, which enables them to function for a longer period [4,6,9–15]. Recently, the

perspective commercial utilization of μ PSC along with their growing power density was reported in [2].

Still, efforts have been made to generate electricity from various photosynthetic microorganisms and photosynthetic pigments such as thylakoid membranes, reaction centers, etc. [5,8,10,16]. Moreover, significant endeavors have been made in engineering design and experimental investigations [5,8,10,16]. Modern research evolved in understanding this green energy for sustainable use over the recent years [17–27].

Modeling such complex systems enables understanding the underlying phenomenon of the device, and it aids in optimizing the metrics of the device [28]. The modeling of this μ PSC is feasible via the coupled solution of the Nernst equation and the Butler–Volmer equation. This approach accounts for the mass transfer across the proton exchange membrane, countering the electrons collected in carefully engineered electrodes. In this regard, attempts have been made in mathematical modeling of the single μ PSC from the first principle approach and electrical equivalent modeling of the single individual μ PSCs [28,29]. This modeling approach resulted in optimizing the operational parameters via proper engineering design. However, for the μ PSC to find application in powering real-time day-to-day applications, it is necessary to improve the power rating of this device via interfacing (arraying) several individual μ PSCs. Modeling and analysis of such arrayed systems are crucial, as they not only result in understanding the dynamics and physics of this system but also fine-tune the metrics of this arrayed μ PSC.

Despite this necessity, the maximum performance of the single μ PSC is limited by thermodynamics. The maximum possible terminal voltage that could be generated from the single μ PSC is only 1.8 V [29]. Therefore, using the μ PSC for real-time applications with a single μ PSC is unfeasible. It is essential to realize the array configurations to obtain the desired voltage and current from the μ PSCs. Few experimental works have been reported in this direction [5]. Nevertheless, to our knowledge, further studies are needed for the modeling of the array of μ PSC.

In this effect, in the current study, electrical equivalent modeling of the array of the μ PSC in several array configurations is presented. The proposed arraying model extends the electrical equivalent model of a single μ PSC [29]. All the parameters and operating conditions were maintained the same as those of the previous single μ PSC. The total area of the electrode was 4.84 cm², and the volume of anolyte (photosynthetic microorganism) and catholyte (potassium ferricyanide) was 2 mL. The array of six μ PSCs was simulated for series, parallel, and combinations of series and parallel configurations, and further, the simulated results were compared with experimental results. The study includes steady-state responses with an external electrical loading of 1 k Ω . Nevertheless, loading conditions could be extended to any electrical load. The polarization characteristics of the current-voltage (I-V) and current-power (I-P) characteristics of the array of μ PSCs in series and parallel and their combinations in series and parallel connected μ PSCs were validated with the experimental results.

2. μ PSC Operation and Fabrication

The principle of operation of the μ PSC is the natural photosynthesis and respiration process. The μ PSC involves the membrane electrode assembly sandwiched between the anode and cathode chambers. In the anode, photosynthesis drives the water-splitting reaction and releases electrons. In contrast, in the respiration process, electrons are also released by the catabolic activity of the photosynthetic microorganisms. These electrons traverse through electrodes in the membrane electrode assembly. Figure 1a demonstrates the principle of operation of the μ PSC. As the detailed principle of operation is presented in our previous works, the authors recommend referring to [3,8,11].

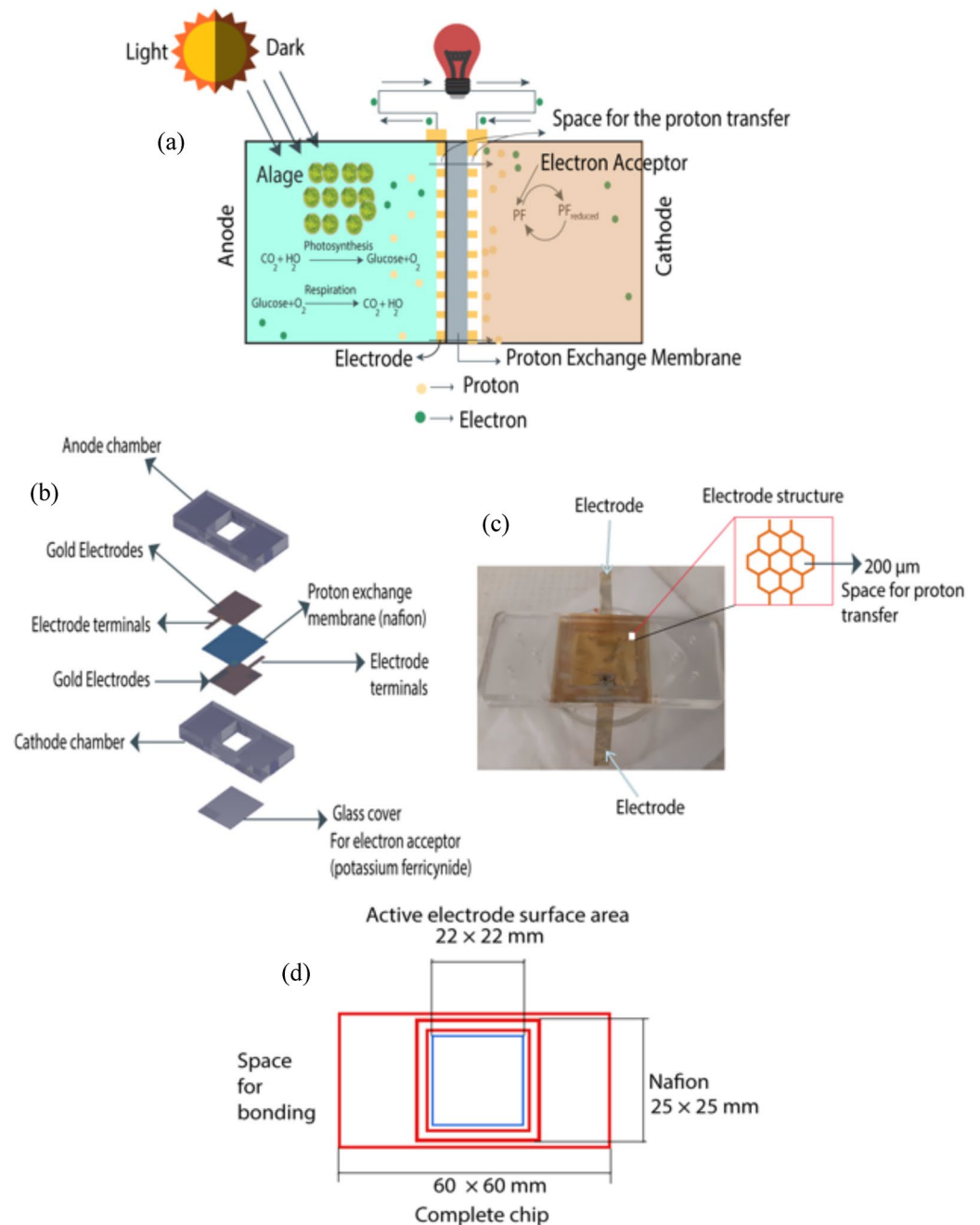
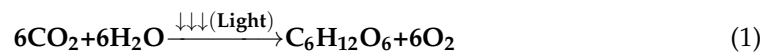


Figure 1. (a) Operating principle, (b) components of the μPSC , (c) photo image of the fabricated μPSC , (d) dimensions of the μPSC .

Photosynthesis



Respiration



3. μPSC Fabrication

The μPSC comprises two chambers: anode and cathode. Both chambers are separated by the proton exchange membrane (PEM). The microelectrodes were fabricated on both sides of the PEM. The microelectrodes comprised a thin aluminum honeycomb-structured arrayed grid coated with 40 nm gold through the sputtering technique. The electrode-patterned PEM

was sandwiched between the anode and cathode chambers. The cathode chamber was sealed with a microscopic glass slide to hold the electron acceptor (potassium ferricyanide). Figure 1b illustrates the various components and assemblies of the μ PSC. Figure 1c shows the photo image of the assembled μ PSC. The detailed dimensions of the whole μ PSC are shown in Figure 1d. As the focus of this work is on the modeling of the μ PSC, for fabrication and experimental details, it is suggested to refer to our previous work [3,8,30]. The micro-photosynthetic power cells have been evaluated under an illumination level of $2 \mu\text{molm}^{-2}\text{s}^{-1}$, which has consistently demonstrated superior performance compared to other lighting conditions. Consequently, all characterizations have been conducted under this specific illumination setting [29].

4. Modeling the Electrical Equivalent Circuit of a Single μ -PSC

The terminal voltage of the μ PSC is the Nernst reversible voltage with μ PSC internal losses such as activation voltage loss, concentration voltage loss, and ohmic voltage loss. Hence, the terminal voltage could be written as

$$V = E_0 - V_{act} - V_{conc} - V_{ohmic} \quad (3)$$

where,

V —Voltage of the μ PSC measured across terminals (V)

E_0 —Nernst reversible voltage (V)

V_{act} , activation voltage loss = $\frac{RT}{\alpha F} \sinh^{-1}\left(\frac{i}{2i_0}\right)$

V_{conc} , concentration voltage loss = $\left(\frac{-RT}{nF} \ln\left(1 - \frac{i}{i_L}\right)\right)$

V_{ohmic} , Ohmic voltage losses = $R_{ohmic}i$

The activation, concentration, and Ohmic losses were directly substituted from the work [29]. where,

R	Universal gas constant (8.31447 J/mol-K)
T	Operating temperature (Room temperature, (298.15 K)
F	Faraday's constant (96,486 C/mol)
n	Number of transferred electrons/reactions (4 mol)
i_L	Limiting current density (0.1818 mA/cm ²)
i_0	Equilibrium exchange current density (10^{-8} A/cm ²)
R_{ohmic}	Ohmic resistance (Ω)

All these parameters are constants [29]. The Nernst Reversible voltage is given by,

$$E_0 = E_{cell}^0 - \frac{RT}{nF} \ln\left(\frac{[Re_{red}]^2 [PF_{red}]^4}{[Re]^4 [H^+]^4 [PF]^4}\right) \quad (4)$$

The anode chamber of the μ PSC consist of anolyte (algal cells with electron mediators' methylene blue). The cathode chamber consists of electron acceptors (potassium ferricyanide). The oxidation and reduction of methylene blue and electron acceptors potassium ferricyanide during the process are the reactants and products.

The electrical equivalent circuit of the single μ PSC is shown in Figure 2a [29]. In the Nernst reversible voltage, E_{cell}^0 of the μ PSC is modelled as DC voltage source and reactants and products were modelled as controlled voltage source, which is the function of the rate of change in the anode and cathode species concentration. The rate of change of species concentration is the solution of a set of first-order differential equations [28]. Both the activation and concentration voltage losses were modeled as controlled voltage sources. The Ohmic loss is represented as the resistive element. The proton exchange membrane is modeled as a capacitor. The resistive load is connected to the terminals of the μ PSC [29].

Figure 2b shows the electrical equivalent model of the two μ PSCs in series connection and Figure 2c shows the electrical equivalent model of the two μ PSCs in parallel connection. Figure 2d shows the electrical equivalent circuit of a combination of series and parallel connections of the μ PSC.

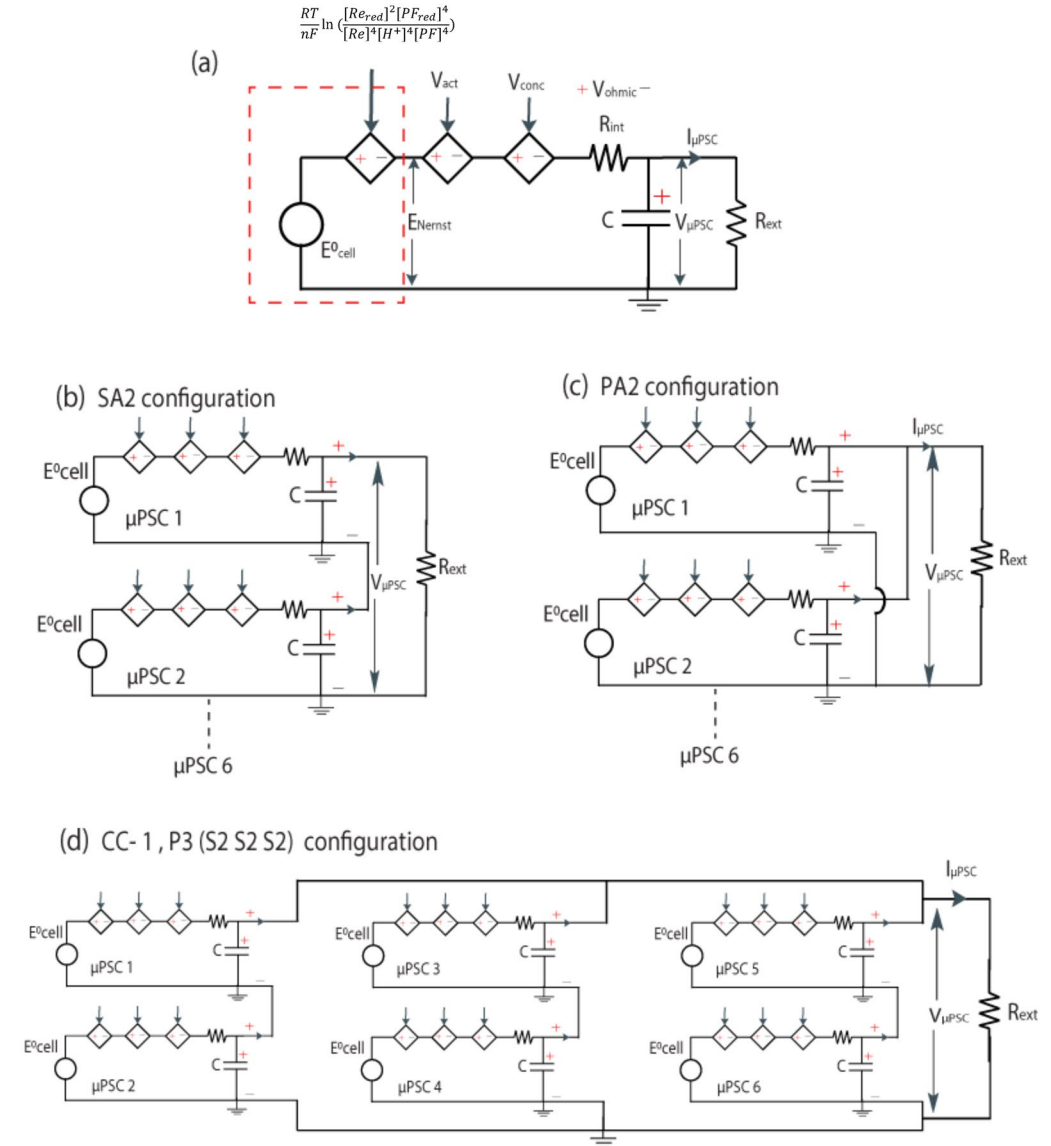


Figure 2. (a) Electrical equivalent circuit of the single μ PSC, (b) equivalent circuit of two μ PSCs in series connection, (c) equivalent circuit of two μ PSCs in parallel connection, (d) equivalent circuit of P3 (S2, S2, S2) configuration.

5. Modeling Array Configurations of μ -PSCs

5.1. SA6 Configuration

In the SA6 configuration, the μ PSCs were connected in series connections. The six μ PSCs were all connected in series (Figure 3a).

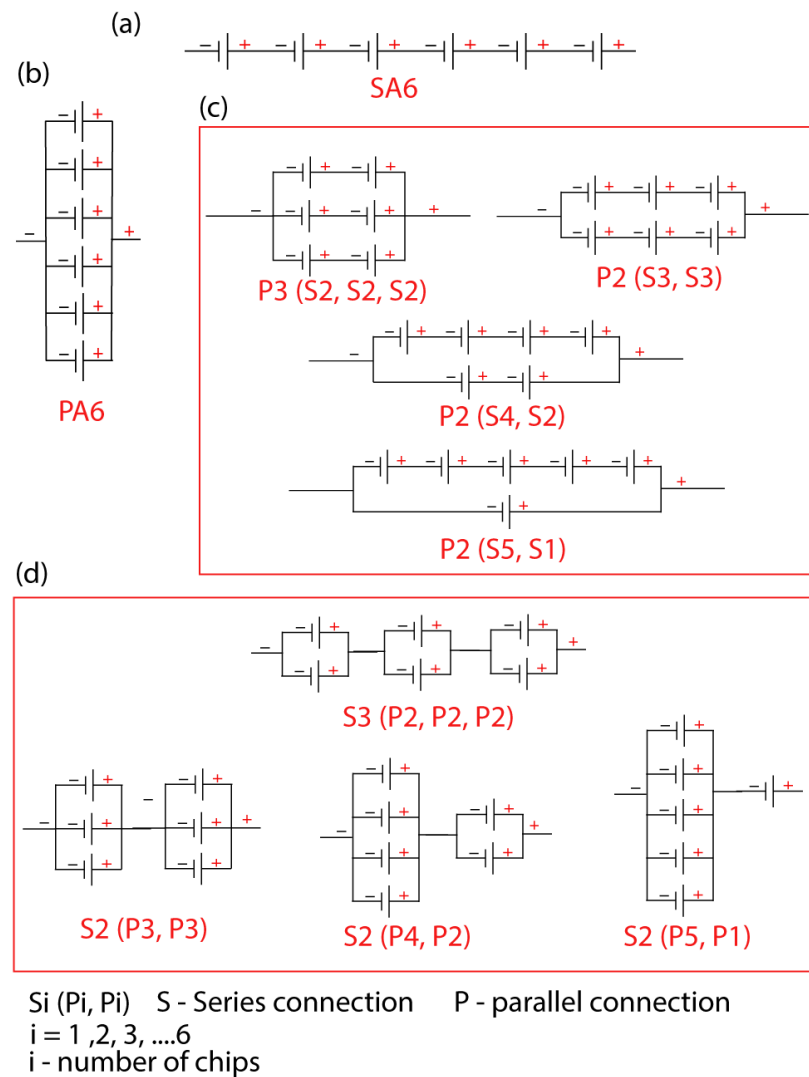


Figure 3. (a) SA6 configuration of μ PSCs (b) PA6 configuration of μ PSCs (c) Combinatory configuration—1 (CC-1) of μ PSCs, four combinations ([P3 (S2, S2, S2)], [P2 (S3, S3)], [P2 (S4, S2)], [P2 (S5, S1)]) (d) combinatory configuration—2 of μ PSCs, four combinations ([S3 (P2, P2, P2)], [S2 (P3, P3)], [S2 (P4, P2)], [S2 (P5, P1)]).

5.2. PA6 Configuration

In the PA6 configuration, the μ PSCs were connected in parallel. The first μ PSCs anode and sixth μ PSCs cathode terminals were connected to the DAQ for the current and voltage sensing (Figure 3b). The photo image of the PA6 configurations is shown in Figure 4a.

5.3. Combinatory Configuration (CC-1)

To observe the performance of the μ PSCs in sequences of series and parallel configurations, four unique configurations were chosen to analyze the performance. In the [P3 (S2, S2, S2)] configuration, two μ PSCs were connected in series, and such three sets were connected in parallel connection (Figure 3c). In other configurations, two sets of three μ PSCs were connected in series; then, both the sets were connected in parallel connection [P2 (S3, S3)]. In [P2 (S4, S2)] configuration, four μ PSCs were connected in series, and separate two μ PSCs were connected in series then both sets were connected in parallel. In [P2 (S5, S1)] configuration, the five μ PSCs were connected in series connection, and single μ PSC were connected in parallel connection.

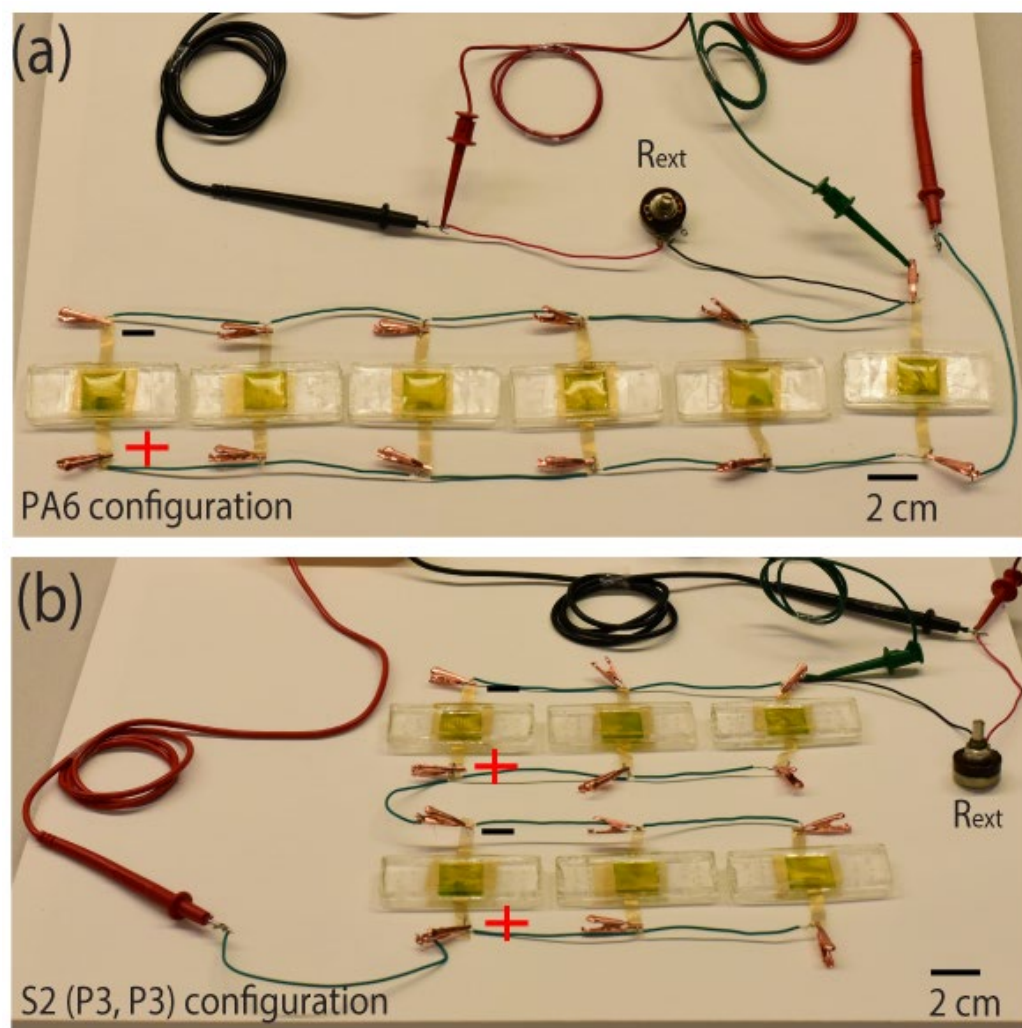


Figure 4. Photo image of the array configurations of the μ PSCs. (a) PA6 configuration (b) S2 (P3,P3) configuration.

5.4. Combinatory Configuration (CC-2)

In the CC-2 configuration four unique configurations were chosen. In the [S3 (P2, P2, P2)] configuration, two μ PSCs were connected in parallel, and three sets of such parallel connections were connected in series connection (Figure 3d). In configuration S2 (P3, P3), two sets of three μ PSCs were connected in parallel, and then both the sets were connected in series connection. A photo image of this configuration is shown in Figure 4b. In S2 (P4, P2) configuration, four μ PSCs were connected in parallel and two μ PSCs were connected in parallel, then both sets were connected in series. In the last CC-2 configuration, five μ PSCs were connected in parallel connection, and single μ PSC were connected in a series connection to that [S2 (P5, P1)].

The experimental performances of the μ PSCs may differ due to variations in the fabrication and also transient parameters such as rate of changes in species concentration, illumination on the surface of the anode chamber, and many more. Therefore, for simplicity and to demonstrate the capacity of the model for the arrayed configurations, normalized values are presented to analyze the I-V and I-P characteristics of the array of the μ PSCs. The normalized voltage of the μ PSC is calculated as, $Vr = \frac{V}{V_{oc}}$, where V is the terminal voltage of the μ PSC and V_{oc} is the open circuit voltage of the μ PSC. The similarly normalized current of the μ PSC is calculated as, $Ir = \frac{I}{I_{sc}}$, where I, is the μ PSC current and I_{sc} is the short circuit current of the μ PSC. The normalized power of the μ PSC is calculated as, $Pr = \frac{P}{P_{mp}}$, where P is the power of the μ PSC and P_{mp} is the maximum power of the μ PSC.

6. Results and Discussion

6.1. Polarization (I-V) Characteristics of SA6 Configuration

The I-V polarization characteristics are vital to comprehending the performance of the power-generating device. The I-V characteristics could be exploited to design suitable power converters for practical applications. Figure 5b demonstrates the normalized I-V characteristics of the SA2 configuration. In the SA2 configuration, the effective terminal voltage was the sum of their terminal voltages (Table 1). In contrast, the effective current remained the same as that of the least μ PSCs current in this array configuration.

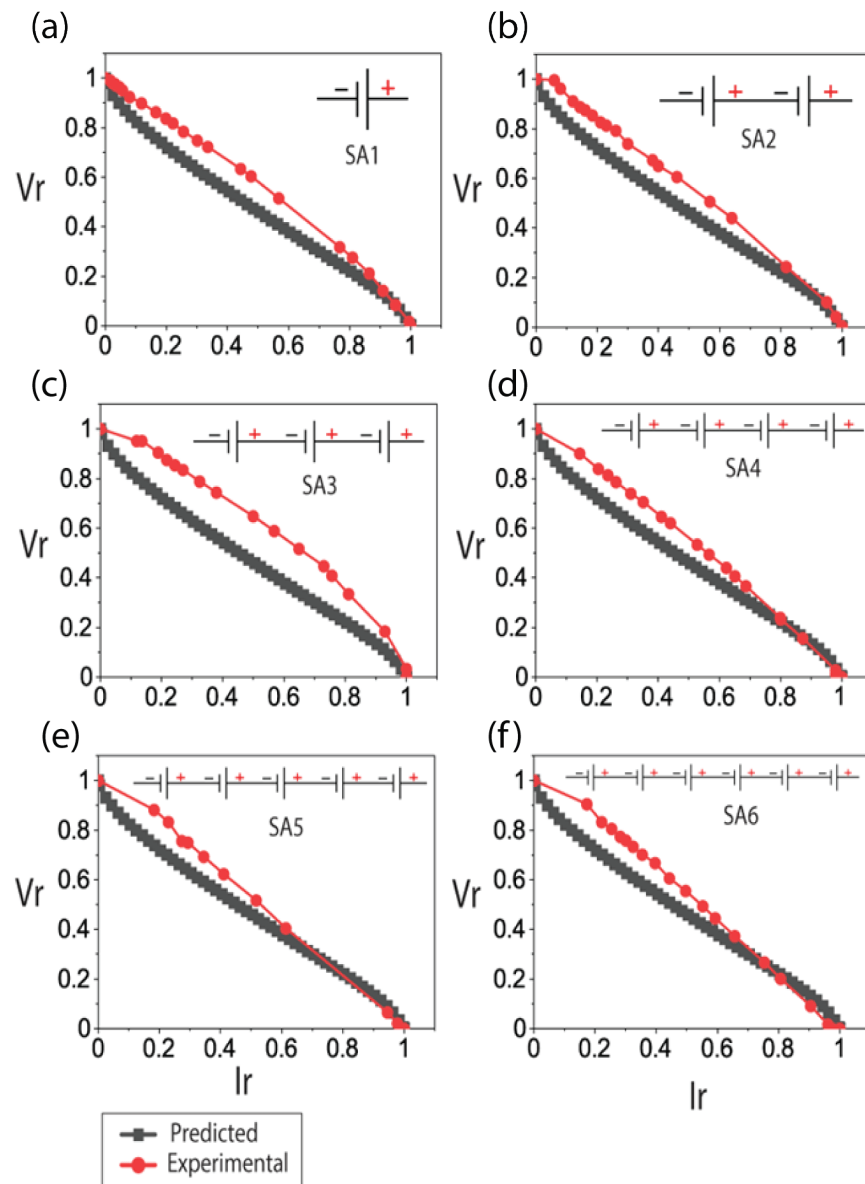


Figure 5. Normalized I-V characteristics of SA6 configuration, (a) SA1 configuration, (b) SA2 configuration, (c) SA3 configuration, (d) SA4 configuration, (e) SA5 configuration, (f) SA6 configuration. Red circle lines represent the experimental results; black squares represent the simulated (predicted values).

Table 1. Real-time predicted and experimental Voc, Isc, and Pmp of SA6 configurations.

Array	(V _{oc}) mV		(I _{sc}) μ A		(P _{mp}) μ W	
	Predicted	Experimental	Predicted	Experimental	Predicted	Experimental
SA1	848.6	780	800	820	180	186
SA2	1697	1404	800	500	314	202
SA3	2545	2101	800	370	472	271
SA4	3394	3000	800	340	629	285
SA5	4243	3700	800	334	786	330
SA6	5091	4200	800	410	944	474

In the model, all of the μ PSCs utilized in array configurations demonstrated consistent performance because of consistent transient parameters. In contrast, the experimental results exhibited distinct performance, mainly because of the inconsistent performances of the μ PSCs due to the uncontrolled transient parameters, which are yet to be understood in detail. Another significant reason for the inconsistent performance is the non-uniformity of the fabrication and transient behaviors [3,8].

Figure 5c reveals the SA3 configuration. In the model in the series configurations, the effective current remained unchanged at 800 μ A, whereas the effective voltage was observed to be the summation of their voltages (Table 1). Figure 5d–f demonstrated the SA4, SA5, and SA6 configurations. Here, similar observations as those of the SA2 and SA3 configurations were also made. In the SA6 configuration, the effective voltage was the sum of their voltages, and the effective current remained the same as those of the least-performing μ PSCs (Table 1).

6.2. Polarization (I-V) Characteristics of PA6 Configuration

Figure S1 demonstrates the normalized I-V characteristics of the PA6 configuration. In parallel configurations, the effective voltages remained identical to those of the least-performing μ PSCs voltage (Table 2). In contrast, the effective current of the configuration was the sum of their μ PSCs currents. For the PA2 configuration, experimental results demonstrated a current of 840 μ A, whereas the predicted current demonstrated 1600 μ A. The lower performance of the current in the experimental results was because of the meager performance of the μ PSC owing to its inconsistent fabrications. The predicted current of 1600 μ A indicated two μ PSCs in parallel could potentially increase the mentioned performance using consistent fabrication of the μ PSCs. Similar observations were made in the PA3, PA4, PA5, and PA6 configurations. Their effective terminal voltages almost remained the same as those of the least-performing μ PSCs voltage. In contrast, their effective current was the sum of their μ PSCs current (Table 2). In the PA6 configuration, a maximum effective voltage of 800 mV and a current of 4800 μ A were predicted.

Table 2. Real-time predicted and experimental Voc, Isc, and Pmp of PA6 configurations.

Array	(V _{oc}) mV		(I _{sc}) μ A		(P _{mp}) μ W	
	Predicted	Experimental	Predicted	Experimental	Predicted	Experimental
PA1	848.6	780	800	820	180	186
PA2	848.6	725	1600	880	314	183.96
PA3	848.6	765	2400	1480	472	308.7
PA4	848.6	675	3200	1700	629	256
PA5	848.6	736	4000	2400	786	496.2
PA6	848.6	730	4800	2600	944	412.5

6.3. Polarization (I-V) Characteristics of CC-1 Configuration

The effective terminal voltages of the μ PSCs were increased in the series configurations, and effective μ PSCs currents remained the least μ PSCs current. In contrast, the effective μ PSC currents were enhanced in the parallel configurations, and their effective voltage remained the least-performing μ PSC. Based on this understanding, to enhance both the effective voltage and effective μ PSCs current of the arrayed μ PSCs different array combinations of series and parallel were chosen.

Figure 6a demonstrates the normalized I-V characteristics of the [P2 (S2, S2, S2)] combination of the CC-1 configuration. The predicted values were slightly greater than the experimental values, indicating that the experimental μ PSC current could be boosted by consistent fabrication (Table 3). In this combination, both effective voltages and currents were enhanced. Figure 6b reveals the normalized I-V characteristics of the [P2(S3, S3)] combination. Herein, the experimental results were almost matching the predicted values, whereas the experimental currents were slightly less than the predicted values. However, it was found that in both of these combinations, voltages and currents were enhanced.

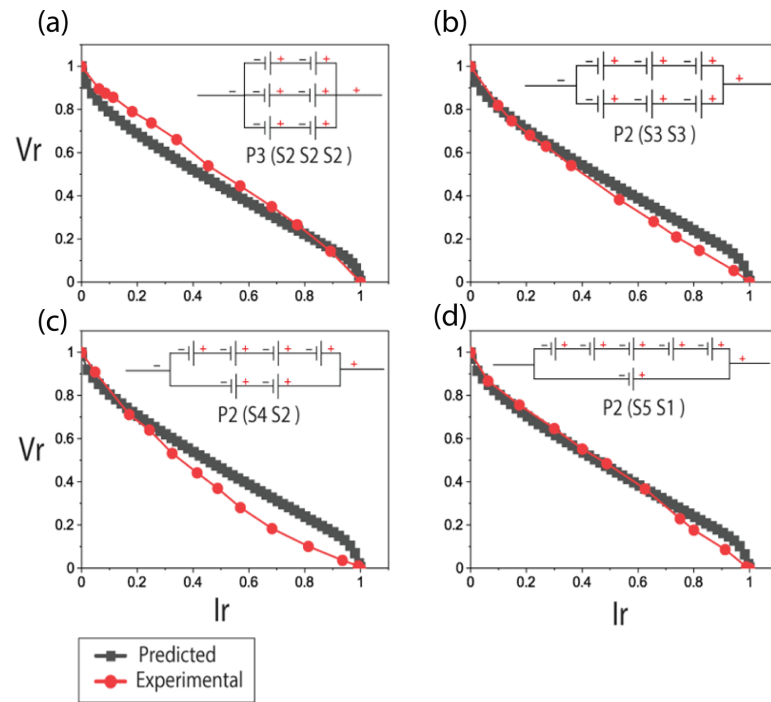


Figure 6. Normalized I-V characteristics of CC-1 configuration. (a) [P2(S2, S2, S2)] configuration (b) [P2(S3, S3)] configuration (c) [P2(S4, S2)] configuration (d) [P2 (S5, S1)] configuration. The red circles represent the experimental results; black squares represent the simulated (predicted values).

Table 3. Real-time predicted and experimental V_{oc} , I_{sc} , and P_{mp} of CC-1 configurations.

CC-1	(V_{oc}) mV		(I_{sc}) μ A		(P_{mp}) μ W	
	P	E	P	E	P	E
P3 (S2,S2,S2)	1839	1550	2400	1760	985	616
P2 (S3,S3)	2741	2430	1600	1220	1026	624
P2 (S4,S2)	2438	2800	1600	1230	912	396
P2 (S5,S1)	1526	1302	1600	800	570	246

Figure 6c shows the normalized I-V characteristics of the [P2 (S4, S2)] configuration. The predicted effective terminal voltages were slightly lower than the experimental value, perhaps because of the increase in the voltage in the long-term performance (Table 3) [10]. Figure 6d shows the normalized I-V characteristics of the [P2 (S5, S1)] configuration. The effective terminal voltages of the experiment were almost close to the predicted values. However, the effective currents of the experiment were quite lower than the predicted ones.

6.4. Polarization (I-V) Characteristics of CC-2 Configuration

To observe the performance of the μ PSCs in combinations of parallel configurations, unique parallel combination strategies were chosen. Their corresponding normalized I-V characteristics were simulated and validated with the experimental results. Figure S2a demonstrates the normalized I-V characteristics of the CC-2 configuration [S2 (P2, P2,

P2)]. Figure S2b demonstrates the [S2 (P3, P3)] configuration. Here, it was observed that experimental terminal currents were slightly higher than the predicted currents, perhaps because of a higher rate of electron transfer to the electrode surface, which is not considered in the modeling (Table 4). Figure S2c shows the [S2 (P4, P2)] configuration. Here too, similar observation was made, like that of the [S2 (P3, P3)] configuration. Figure S2d shows the normalized I-V characteristics of the [S2 (P5, P1)].

Table 4. Real time predicted and experimental Voc, Isc, and P_{mp} of CC-2 configurations.

CC-2	(V _{oc})		(I _{sc})		(P _{mp})	
	P	E	P	E	P	E
S3 (P2, P2, P2)	2741	2300	1600	1390	1026	869
S2 (P3, P3)	1839	1475	2400	2100	985	926
S2 (P4, P2)	1833	1680	1600	1820	887	777
S2 (P5, P1)	1826	1530	800	960	561	141

6.5. I-P Characteristics

The current—Power (I-P) characteristics provide the maximum power of the typical power generating device—these aid to design the appropriate power converters for maximum power enhancement. Figure 7 demonstrates the normalized I-P characteristics of the μ PSC array configurations.

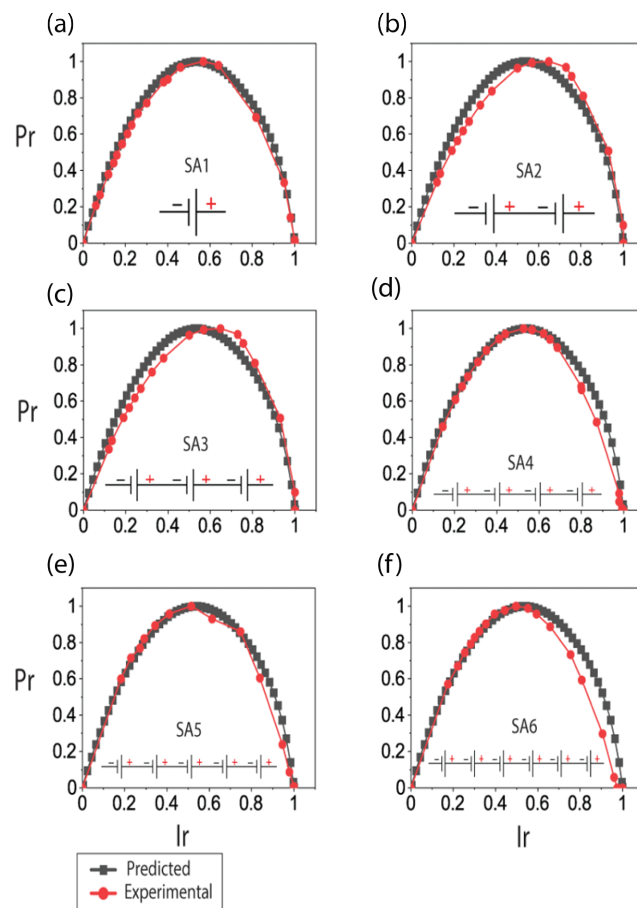


Figure 7. Normalized I-P characteristic curves SA6 configuration. (a) SA1 configuration, (b) SA2 configuration, (c) SA3 configuration, (d) SA4 configuration, (e) SA5 configuration, (f) SA6 configuration. The circles represent the experimental results; black squares represent the simulated (predicted values).

6.6. I-P Characteristics of SA6 Configuration

Figure 7b demonstrates the normalized I-P characteristic of the SA2 configuration. The predicted values indicate that the experimental power could be enhanced up to the maximum potential predicted by the modeling for the said dimensions (Table 1). Similar observations were made with the SA3, SA4, SA5, and SA6 configurations. From the simulation, it was realized that by adding a greater number of μ PSCs in series, its power output could be enhanced. The enhancement factor follows the linear relationship, provided all the μ PSCs in that configuration have the same performance (Table 1). One of the μ PSC's lower performances leads to lower effective performance. In all the SA6 configurations, the current has remained the same, and the voltage increased with an increase in the number of μ PSCs. The increase in the voltage has led to increased power output in the SA6 configuration.

6.7. I-P Characteristics of PA6 Configuration

Figure S3b demonstrates the normalized I-P characteristic PA2 configuration. The predicted maximum power indicated that in the parallel connection, both current and power could be enhanced by increasing the number of μ PSCs. The similar observations were made in PA3 (Figure S3c), PA4 (Figure S3d), PA5 (Figure S3e) and PA6 (Figure S3f) configuration.

6.8. I-P Characteristics of CC-1 Configuration

Figure S5a demonstrates the normalized I-P characteristics of the [P2 (S2, S2, S2)] configuration. Compared to the SA6 and PA6 configurations, the combination of series and parallel μ PSCs has demonstrated higher maximum power. In this array configuration, the model has predicted a maximum power (P_{mp}) of 1000 μ W, indicating the maximum power that could be potentially generated by this array configuration. Similar observations were made with [P2 (S3, S3)] (Figure S5b), [P2 (S4, S2)] (Figure S5c) and P2 (S5, S1) (Figure S5d) configurations.

6.9. I-P Characteristics of CC-2 Configuration

Figure S4a demonstrates the normalized I-P characteristics of the CC-2 configuration's [S2 (P2, P2, P2)] configuration. Compared to all other configurations, the [S2 (P2, P2, P2)] configuration has generated higher maximum power than any other combination. In the case of combination [S2 (P4, P2)] and [S2 (P5, P1)], the experimental currents were slightly greater than the predicted values, perhaps because of the higher rate of electron transport in the long-term performance of the μ PSCs, which was not considered in the modeling (Table 4).

The combinations [S2 (P4, P2)] (Figure S4c) and [S2 (P5, P1)] (Figure S4d) have shown a slightly different pattern than the other combinations. Both experimental and predicted I-P characteristics showed slightly different patterns, which perhaps indicates slightly different phenomena with these combinations. More investigations are necessary to understand the underlying phenomenon of this combination. Moreover, both combinations' effective terminal voltage and currents were much lower than all other combinations in this study.

6.10. Variation of Open-Circuit Voltage (V_{oc}), Short Circuit Current (I_{sc}), Load Voltage (V_L), and Load Current (I_L)

6.10.1. Variation of Open-Circuit Voltage (V_{oc})

In the case of the SA6 configuration, the model has predicted slightly higher values than the experimental values, indicating the experimental values could be potentially enhanced by the consistent performances of all the μ PSCs in an array configuration. In the SA2 configuration, experimental values have demonstrated a slightly lower V_{oc} of 1404 mV compared to the predicted value of 1697 mV. In the SA3 configuration, experimental values have demonstrated a V_{oc} of 2101 mV, while the model has predicted 2550 mV. It was observed that with an increase in the number of μ PSCs in series connection, the losses

(ohmic) in the circuit have increased. This indicates that the Voc of the effective array of μ PSCs in series connections is the summation of the individual Voc with ohmic losses in the circuit.

In the PA6 configuration, the effective Voc was the result of the least-performing μ PSC's Voc. Here, the predicted values remained at 848. A total of 8 mV, while the experimental values varied in the range of 675 mV to 765 mV. However, the variation is insignificant.

The experimental values of [P2 (S2,S2,S2)], [P2 (S3,S3)], and [P2 (S5,S1)] were slightly less than the predicted values. In these combinations, the difference between experimental and predicted values was insignificant. The combination [P2 (S4, S2)] has predicted a slightly lower Voc than the experimental value, perhaps because, in the long run, the Voc has increased during the experimental section.

The combination [S2 (P2, P2, P2)] has demonstrated a higher Voc than the experimental value, indicating the possibility of improving the performance of the μ PSC with consistent performance. In all other combinations, the experimental values were slightly less than the predicted values.

6.10.2. Variation of Short Circuit Current (Isc)

In the SA6 configuration, the effective Isc has remained the least-performing μ PSC Isc. The predicted Isc has remained at 800 μ A in all series configurations of μ PSCs. Theoretically, the experimental values should be closer to the predicted values; however, due to the inconsistent performance of the μ PSCs, the experimental results demonstrated slightly lesser values (Table 1).

In a parallel connection, effective Isc was the summation of the individual Isc of the μ PSCs. The two μ PSCs in parallel connection have a predicted Isc of 1600 μ A. It was observed that as the number of μ PSCs increased in the parallel connection, the Isc increased. It was the linear summation of the individual μ PSCs Isc (Table 2).

The combination [P2 (S2, S2, S2)] has demonstrated a difference of 480 μ A from their predicted values. The combination [P2 (S3, S3)] has demonstrated a 300 μ A lesser value than their predicted values. Similar observations were made with [P2 (S4, S2)]. Only the combination [P2 (S5, S1)] has shown a higher difference of 800 μ A compared to their predicted values. It was observed that these combinations generated near values similar to those of their corresponding predicted values.

The [S2 (P2, P2, P2)] has shown a slight difference of 220 μ A compared to their predicted value of 1600 μ A. The combination [S2 (P3, P3)] has demonstrated a difference of 200 μ A from their predicted values. The combination [P2 (S4, S2)] has a slightly higher experimental Isc than the predicted values. The combination [P2 (S5, S1)] has also shown a slightly higher experimental value than predicted values. The main reason might be μ PSCs dynamics. During the dynamics, their performance may have increased, as in the long run, the μ PSCs performance increases. Furthermore, these operation dynamics were not considered in the modeling.

6.10.3. Variation of Load Voltage (V_L) and Current (I_L) at 1 k Ω

To observe the performance of μ PSC under real-time loading conditions, a load test at 1 k Ω was simulated for all array configurations. The resistance of 1 k Ω was connected to the terminals of the μ PSC, and their corresponding terminal voltage and currents were recorded. Further, their predicted results were compared with experimental results.

The μ PSC follows the ohms law. When the load resistance was set to 1 k Ω , their voltages and currents were the same. Therefore, separate load currents were not provided. The V_L and I_L were provided in mV and μ A, respectively.

Figure S6a illustrates the V_L of the SA6 configuration. For all six μ PSCs in series connection, the model has predicted a V_L of 661 mV. However, the experimental values varied in the range of 322 to 370 mV due to variations in their performances. The number of μ PSCs increased, but their V_L was not increased, indicating that for real-time loading

conditions, these connections are ineffective. Similar observations were made with load currents as well, and currents are in μA .

Figure S6b shows the V_L of the PA6 configuration. The parallel-connected μPSCs have demonstrated a higher V_L than the series-connected μPSCs . The two μPSCs in parallel configurations have demonstrated a V_L of 450 mV, whereas the model has predicted 559 mV. In this configuration, an increase in the V_L was observed with an increase in the number of μPSCs in parallel connection. For PA3 configuration, the model has predicted a V_L of 605 mV, and with PA6 configuration, the model has predicted a V_L of 660 mV. With an increase in the number of μPSCs in parallel connection, V_L was found to be increased. A similar trend was observed with experimental results too. As the number of μPSCs increased in the parallel configurations, their corresponding V_L increased. Though there are some discrepancies in the values, the overall trend increased with an increase in the number of μPSCs in parallel connection, and therefore, compared to the series connection of μPSCs , parallel configurations have a slightly increasing trend with an increase in the number of μPSCs .

Figure S6c illustrates the V_L of CC-1 configurations. For the combination [P2 (S2, S2, S2)], the model has predicted a higher V_L than the series (SA6) and parallel (PA6) configurations. This combination has predicted a V_L of 1039 mV, whereas the experimental values demonstrated a value of 800 mV. The difference of 239 mV is perhaps because of the ohmic losses and inconsistent performances of the μPSCs in the array configurations. For the combination [P2 (S3, S3)], the model has predicted a V_L of 909 mV, whereas the experimental value has demonstrated a value of 800 mV. The combination of [P2 (S4, S2)] and [P2 (S5, S1)] experimental and predicted values is shown in Figure S6c. In all the combinations, it was observed that the predicted V_L was much higher than the experimental values of series and parallel configurations.

Figure S6d shows the CC-2 configuration μPSCs . Here it was found that the experimental V_L was much higher than the predicted values, perhaps because μPSC has shown an increasing trend with long-term operation. The long-term performance dynamics are not included in the modeling.

Among all these four different array configurations, it was found that the CC-1 and CC-2 configurations have demonstrated higher V_L and I_L than the only series and parallel connected μPSCs . Therefore, for real-time loading conditions, the combinations of series and parallel connections were considered the optimal strategies.

6.10.4. Variation of Maximum Power (P_{mp}) of Array Configurations

P_{mp} is the highest power generated from the μPSCs . Figure 8a demonstrates the P_{mp} of an array of μPSCs in the SA6 configuration. According to the model, it was observed that the maximum power increased with an increase in the number of μPSCs in the series connection. For the SA2 configuration, the model has predicted a P_{mp} of 359.9 μW , whereas the experimental value has shown 202.2 μW (Table 1). The lower experimental value was mostly perhaps because of the inconsistent performances of the μPSCs and ohmic losses in the circuit. The six μPSCs in series connection have a predicted P_{mp} of 1079.9 μW . Overall, in the series connection of μPSC , the P_{mp} has observed an increasing trend.

Figure 8b shows the P_{mp} of the PA6 configuration. Also, with an increase in the number of μPSCs , an increase in the P_{mp} was observed. For six μPSCs in parallel connection, the model has predicted a P_{mp} of 908.2 μW . Overall, an increase in the number of μPSCs in parallel connections was observed. However, series-connected μPSCs have demonstrated a slightly higher P_{mp} compared to parallel-connected μPSCs .

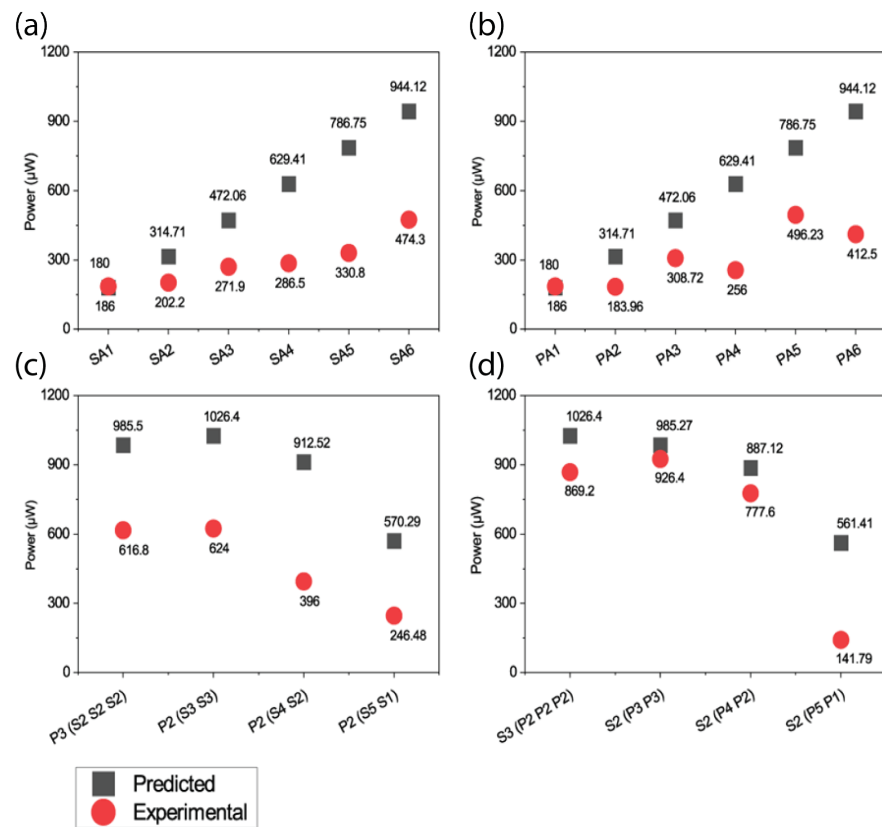


Figure 8. Variation of P_{mp} of predicted and experimental results of all four array configurations. (a) SA6 configuration, (b) PA6 configuration, (c) CC-1 configuration, (d) CC-2 configuration.

Figure 8c shows the P_{mp} of CC-1 configurations. For the combination [P2 (S2, S2, S2)], the model has predicted a P_{mp} of 985.5 μW , whereas the experimental values have demonstrated 616.8 μW . The combination [P2(S3, S3)] has predicted a P_{mp} of 1026.4 μW , and whereas the experiment has demonstrated 624 μW . The combination [P2(S4, S2)] and [P2 (S5, S1)] has predicted a slightly lower P_{mp} than the experimental values.

Figure 8d shows the P_{mp} of the CC-2 configuration. The combination [S2 (P2, P2, P2)] has predicted a P_{mp} of 1026.4 μW , whereas the experimental results have demonstrated a closer value of 869.2 μW . The combination [S2 (P3, P3)] model has predicted 985.27 μW . In contrast, the experimental values have predicted a value of 926.4 μW , which is close to the predicted one. For the combinations [S2 (P4, P2)] and [S2 (P5, P1)], the model has predicted values lower than the other two combinations.

In the comparison of P_{mp} , V_L , and I_L currents at 1 k Ω amongst all the array configurations, it was found that CC-1 and CC-2 configurations that too combinations [P2 (S2, S2, S2)], [P2 (S3, S3)] and [S2 (P2, P2, P2)], [S2 (P3, P3)] have demonstrated higher performance both experimentally and with predicted ones. From the model, it is understood that these configurations could be utilized for real-time applications where one can increase both voltages and currents.

6.11. Fill Factor (FF)

Fill factor is the ratio of maximum power obtained by the μPSC to the product of open circuit voltage and short circuit current of the μPSC .

$$\text{Fill factor (FF)} = \frac{P_{mp}}{(V_{oc} \times I_{sc})} \quad (5)$$

Figure S7 shows the I-V and I-P characteristics demonstrating the fill factor. The FF of all the predicted array configurations is calculated and presented in Table 5.

Table 5. Fill factor of all array configurations.

Array	FF	Array	FF
SA1	0.267	PA1	0.267
SA2	0.245	PA2	0.233
SA3	0.236	PA3	0.234
SA4	0.238	PA4	0.234
SA5	0.233	PA5	0.233
SA6	0.236	PA6	0.234
S3 (P2, P2, P2)	0.237	P3 (S2, S2, S2)	0.228
S2 (P3, P3)	0.228	P2 (S3, S3)	0.237
S2 (P4, P2)	0.307	P2 (S4, S2)	0.237
S2 (P5, P1)	0.389	P2 (S5, S1)	0.237

Table 5 shows the FF of the SA6 configurations. It was observed that the FF of the SA6 configurations varied from 0.233 to 0.267. For the single μ PSC, FF was found to be 0.267. In contrast, the FF for the SA2 configurations was observed as 0.245. For SA3, SA4, SA5, and SA6 configurations FF variations are insignificant. Similar observations were made with PA6 and CC-1 configurations too. Here also the variation is insignificant. However, in CC-2, S2 (P4, P2) configuration FF was found to be 0.307. In S2 (P5, P1), configuration FF was found to be 0.389. Amongst all of the array configurations, the CC-1 P3 (S2, S2, S2) configuration and the CC-2 S2 (P3, P3) configuration have shown the lowest FF of 0.228. A maximum power of 985 μ W was predicted with these configurations. In addition, the conversion efficiency of the micro-photosynthetic power cell, which is discussed in this manuscript, has a light input to electricity conversion efficiency of 0.18%. This is smaller in comparison with conventional photovoltaic cells. However, the micro-photosynthetic power cell is in its infancy stage. With advancements in technology, conversion efficiency will improve. Detailed research on the conversion efficiency of light energy to electricity is published in our previous works [15]. Moreover, comparing conventional photovoltaic (PV) solar cells, typically silicon-based, with bio-solar cells involves evaluating their energy conversion efficiencies and operation lifetimes. Conventional silicon-based PV cells exhibit higher efficiencies, ranging from 15% to 22%, with monocrystalline panels being the most efficient (around 20–22%). These cells are renowned for their long-term stability, often maintaining efficiency for over 25 years. In contrast, bio-solar cells, employing biological materials like algae or bacteria, generally achieve lower efficiencies (0.1% to 8%) and face challenges due to the limitations of biological organisms and sensitivity to environmental factors. Operational lifetimes for bio-solar cells are still a subject of research and development, while silicon-based PV panels are known for their durability and established warranties of 25 years or more.

7. Conclusions

This study presents a comprehensive investigation into the performance of array configurations of micro-photosynthetic power cells (μ PSCs). Through rigorous modeling and experimental validation, we explored various array configurations, including series, parallel, and combinations thereof, under real-time loading conditions. Our findings reveal that combinations of series and parallel arrays of μ PSCs are more effective in generating optimal power compared to configurations that utilize solely series or parallel connections. This insight is crucial for the practical application of μ PSCs in powering low- and ultra-low-power devices. The study's primary contribution lies in the proposed model's versatility and applicability across various array configurations, enabling a deeper understanding of the performance characteristics of μ PSC arrays. The polarization characteristics, current-voltage (I-V), and current-power (I-P) profiles of these arrays were validated against experimental results, affirming the model's robustness. Furthermore, the study's findings indicate that the devised array configurations, particularly those combining series and parallel arrangements, are promising for real-time applications where a balance of voltage

and current is essential. This research not only advances the understanding of μ PSCs in array configurations but also paves the way for future studies focusing on optimizing these systems for practical energy harvesting applications. The integration of μ PSCs into the realm of sustainable energy sources represents a significant stride forward, potentially impacting various sectors reliant on low-power solutions. Further research is required to enhance the efficiency and stability of these bio-inspired energy systems, ensuring their viability in real-world applications.

Supplementary Materials: The following supporting information can be downloaded at: <https://www.mdpi.com/article/10.3390/en17071749/s1>, Figure S1: Normalized I-V characteristics of PA6 configuration (a) PA1 configuration (b) PA2 configuration (c) PA3 configuration (d) PA4 configuration (e) PA5 configuration (f) PA6 configuration. The red circles represent the experimental results; black squares represent the simulated (predicted results); Figure S2: Normalized I-V characteristics of CC-2 configuration (a) [S2(P2, P2, P2)] configuration (b) [S2(P3, P3)] configuration (c) [S2(P4, P2)] configuration (d) [S2(P5, P1)] configuration. The red circles represent the experimental results; black squares represent the simulated (predicted values); Figure S3: Normalized I-P characteristics of the PA6 configuration (a) PA1 configuration (b) PA2 configuration (c) PA3 configuration (d) PA4 configuration (e) PA5 configuration (f) PA6 configuration. The red circles represent the experimental results; black squares represent the simulated (predicted values); Figure S4: Normalized I-P characteristics of CC-2 configuration (a) [S2 (P2, P2, P2)] configuration (b) [S2 (P3, P3)] configuration (c) [S2 (P4, P2)] configuration (d) [S2 (P5, P1)] configuration. The red circles represented the experimental results; black squares represent the simulated (predicted values). All the scales are different to show the variation clearly; Figure S5: Normalized I-P characteristics of CC-1 configuration. (a) [P2 (S2, S2, S2)] configuration (b) [P2 (S3, S3)] configuration (c) [P2 (S4, S2)] configuration (d) [P2 (S5, S1)] configuration. The red circles represent the experimental results; black squares represent the simulated (predicted values); Figure S6: Variation of VL of predicted and experimental results of all four array configurations. (b) SA6 configuration (b) PA6 configuration (c) CC-1 configuration (d) CC-2 configuration; Figure S7: Fill factor of the μ PSC.

Author Contributions: Validation, K.K.; Formal analysis, K.K.; Writing—original draft, K.K.; Writing—review & editing, D.M.P.; Visualization, K.K.; Supervision, S.S.P. and M.P.; Funding acquisition, M.P. All authors have read and agreed to the published version of the manuscript.

Funding: This research was funded by the Natural Sciences and Engineering Research Council, grant number N00866.

Data Availability Statement: Data are contained within the article and Supplementary Materials.

Acknowledgments: Authors acknowledge NSERC and FQRNT research funding of M. Packirisamy.

Conflicts of Interest: The authors declare no conflict of interest.

References

1. Dresselhaus, M.S.; Thomas, I.L. Alternative energy technologies. *Nature* **2001**, *414*, 332–337. [[CrossRef](#)] [[PubMed](#)]
2. Kuruvinaashetti, K.; Guoqing, G.; Haobin, J.; Packirisamy, M. Perspective—Application of Micro Photosynthetic Power Cells for IoT in Automotive Industry. *J. Electrochem. Soc.* **2020**, *167*, 037545. [[CrossRef](#)]
3. Tanneru, H.K.; Kuruvinaashetti, K.; Pillay, P.; Rengaswamy, R.; Packirisamy, M. Perspective—Micro photosynthetic power cells. *J. Electrochem. Soc.* **2019**, *166*, B3012. [[CrossRef](#)]
4. Saar, K.L.; Bombelli, P.; Lea-Smith, D.J.; Call, T.; Aro, E.M.; Müller, T.; Howe, C.J.; Knowles, T.P. Enhancing power density of biophotovoltaics by decoupling storage and power delivery. *Nat. Energy* **2018**, *3*, 75–81. [[CrossRef](#)]
5. Sawa, M.; Fantuzzi, A.; Bombelli, P.; Howe, C.J.; Hellgardt, K.; Nixon, P.J. Electricity generation from digitally printed cyanobacteria. *Nat. Commun.* **2017**, *8*, 1327. [[CrossRef](#)]
6. Bombelli, P.; Müller, T.; Herling, T.W.; Howe, C.J.; Knowles, T.P.J. A High Power-Density, Mediator-Free, Microfluidic Biophotovoltaic Device for Cyanobacterial Cells. *Adv. Energy Mater.* **2015**, *5*, 1401299. [[CrossRef](#)]
7. McCormick, A.J.; Bombelli, P.; Bradley, R.W.; Thorne, R.; Wenzel, T.; Howe, C.J. Biophotovoltaics: Oxygenic photosynthetic organisms in the world of bioelectrochemical systems. *Energy Environ. Sci.* **2015**, *8*, 1092–1109. [[CrossRef](#)]
8. Ramanan, A.V.; Pakirisamy, M.; Williamson, S.S. Advanced Fabrication, Modeling, and Testing of a Microphotosynthetic Electrochemical Cell for Energy Harvesting Applications. *IEEE Trans. Power Electron.* **2015**, *30*, 1275–1285. [[CrossRef](#)]

9. Ravi, S.K.; Yu, Z.; Swainsbury, D.J.; Ouyang, J.; Jones, M.R.; Tan, S.C. Enhanced output from biohybrid photoelectrochemical transparent tandem cells integrating photosynthetic proteins genetically modified for expanded solar energy harvesting. *Adv. Energy Mater.* **2017**, *7*, 1601821. [[CrossRef](#)]
10. Driver, A.; Bombelli, P. Biophotovoltaics. *Catalyst*. **2011**, 13–15.
11. Bradley, R.W.; Bombelli, P.; Rowden, S.J.; Howe, C.J. Biological photovoltaics: Intra- and extra-cellular electron transport by cyanobacteria. *Biochem. Soc. Trans.* **2012**, *40*, 1302–1307. [[CrossRef](#)] [[PubMed](#)]
12. Yang, Y.; Gobeze, H.B.; D'Souza, F.; Jankowiak, R.; Li, J. Plasmonic enhancement of biosolar cells employing light harvesting complex II incorporated with core-shell metal@TiO₂ nanoparticles. *Adv. Mater. Interfaces* **2016**, *3*, 1600371. [[CrossRef](#)]
13. Robinson, M.T.; Armbruster, M.E.; Gargye, A.; Cliffl, D.E.; Jennings, G.K. Photosystem I multilayer films for photovoltage enhancement in natural dye-sensitized solar cells. *ACS Appl. Energy Mater.* **2018**, *1*, 301–305.
14. Wey, L.T.; Bombelli, P.; Chen, X.; Lawrence, J.M.; Rabideau, C.M.; Rowden, S.J.; Zhang, J.Z.; Howe, C.J. The development of biophotovoltaic systems for power generation and biological analysis. *ChemElectroChem* **2019**, *6*, 5375–5386. [[CrossRef](#)] [[PubMed](#)]
15. Kuruvinashetti, K.; Pakkiriswami, S.; Packirisamy, M. Gold Nanoparticle interaction in algae enhancing quantum efficiency and power generation in microphotosynthetic power cells. *Adv. Energy Sustain. Res.* **2022**, *3*, 2100135. [[CrossRef](#)]
16. Lam, K.B.; Irwin, E.F.; Healy, K.E.; Lin, L. Bioelectrocatalytic self-assembled thylakoids for micro-power and sensing applications. *Sens. Actuators B Chem.* **2006**, *117*, 480–487. [[CrossRef](#)]
17. Firoozabadi, H.; Mardanpour, M.M.; Motamedian, E. A system-oriented strategy to enhance electron production of *Synechocystis* sp. PCC6803 in bio-photovoltaic devices: Experimental and modeling insights. *Sci. Rep.* **2021**, *11*, 12294. [[CrossRef](#)]
18. Ng, F.-L.; Phang, S.-M.; Periasamy, V.; Beardall, J.; Yunus, K.; Fisher, A.C. Algal biophotovoltaic (BPV) device for generation of bioelectricity using *Synechococcus elongatus* (Cyanophyta). *J. Appl. Phycol.* **2018**, *30*, 2981–2988. [[CrossRef](#)]
19. Kim, M.J.; Bai, S.J.; Youn, J.R.; Song, Y.S. Anomalous power enhancement of biophotovoltaic cell. *J. Power Sources* **2019**, *412*, 301–310. [[CrossRef](#)]
20. Park, S.H.; Song, Y.S. Carbon nanofluid flow based biophotovoltaic cell. *Nano Energy* **2021**, *81*, 105624. [[CrossRef](#)]
21. Carbas, B.B.; Güler, M.; Yücel, K.; Yildiz, H.B. Construction of novel cyanobacteria-based biological photovoltaic solar cells: Hydrogen and photocurrent generated via both photosynthesis and respiratory system. *J. Photochem. Photobiol. Chem.* **2023**, *442*, 114764. [[CrossRef](#)]
22. Choi, D. Developing Sustainable Water and Electricity for Impoverished Regions using Algae-based Bio-Photovoltaics. Available online: https://www.gcrsef.org/wp-content/uploads/formidable/13/State-Research-Paper_Dorothy-Choi.pdf (accessed on 2 October 2023).
23. Chin, J.-C.; Khor, W.-H.; Chong, W.W.F.; Wu, Y.-T.; Kang, H.-S. Effects of anode materials in electricity generation of microalgal-biophotovoltaic system—Part I: Natural biofilm from floating microalgal aggregation. *Mater. Today Proc.* **2022**, *65*, 2970–2978. [[CrossRef](#)]
24. Amjadian, S.; Esmaeilzadeh, M.; Ajeian, R.; Riazi, G.; Ramakrishna, S. Efficiency Enhancement of Biophotovoltaic Solid-State Solar Cells. *Energy Technol.* **2023**, *11*, 2300337. [[CrossRef](#)]
25. Lee, S.J.; Song, J.J.; Lee, H.J.; Jeong, H.Y.; Song, Y.S. Enhanced energy harvesting in a bio-photovoltaic cell by integrating silver nanoparticles. *J. Korean Phys. Soc.* **2022**, *80*, 420–426. [[CrossRef](#)]
26. Liu, L.; Choi, S. Self-sustainable, high-power-density bio-solar cells for lab-on-a-chip applications. *Lab. Chip* **2017**, *17*, 3817–3825. [[CrossRef](#)] [[PubMed](#)]
27. Indro, M.N.; Maddu, A.; Eviana, E. Utilization of cyanobacteria in photovoltaic technology. *IOP Conf. Ser. Earth Environ. Sci.* **2019**, *299*, 012064. [[CrossRef](#)]
28. Tanneru, H.K.; Suresh, R.; Rengaswamy, R. On modeling and optimization of micro-photosynthetic power cells. *Comput. Chem. Eng.* **2017**, *107*, 284–293. [[CrossRef](#)]
29. Masadeh, M.A.; Kuruvinashetti, K.; Shahparnia, M.; Pillay, P.; Packirisamy, M. Electrochemical Modeling and Equivalent Circuit Representation of a Microphotosynthetic Power Cell. *IEEE Trans. Ind. Electron.* **2017**, *64*, 1561–1571. [[CrossRef](#)]
30. Kuruvinashetti, K.; Tanneru, H.K.; Pillay, P.; Packirisamy, M. Review on Microphotosynthetic Power Cells—A Low-Power Energy-Harvesting Bioelectrochemical Cell: From Fundamentals to Applications. *Energy Technol.* **2021**, *9*, 2001002. [[CrossRef](#)]

Disclaimer/Publisher's Note: The statements, opinions and data contained in all publications are solely those of the individual author(s) and contributor(s) and not of MDPI and/or the editor(s). MDPI and/or the editor(s) disclaim responsibility for any injury to people or property resulting from any ideas, methods, instructions or products referred to in the content.